Contents lists available at ScienceDirect

Transportation Geotechnics

journal homepage: www.elsevier.com/locate/trgeo

Assessing the risk of slope failure to highway infrastructure using automated time-lapse electrical resistivity tomography monitoring

Jim Whiteley [a,b,1,*], Cornelia Inauen [c], Paul Wilkinson [a], Philip Meldrum [a], Russell Swift [a], Oliver Kuras [a], Jonathan Chambers [a,*]

[a] Shallow Geohazards and Earth Observation, British Geological Survey, Nottingham, UK
[b] AtkinsRéalis, Two Chamberlain Square, Birmingham, UK
[c] Alfred Wegener Institute, Helmholtz Centre for Polar and Marine Research, Potsdam, Germany

ABSTRACT

Electrical resistivity tomography (ERT) monitoring provides time-lapse images of the subsurface. These images can be used to assess spatiotemporal variation in moisture content, which is a key driver of slope failure, making ERT monitoring an effective tool to evaluate precursory conditions of failure. This work presents the results of ERT monitoring on a slope above a major highway located on the border between England and Wales. During highway construction in the 1960s the slope was subject to several large landslide events which resulted in the re-design of the carriageway and installation of engineered mitigation measures. A section of the slope known as the 'partially slipped area' exhibited partial displacement during this time but did not progress to full slope failure, and therefore presents an ongoing risk to the highway, even though it does not experience ongoing displacement. An ERT monitoring system was installed across this area to monitor subsurface variations in moisture content. The results show a complex pattern of subsurface moisture dynamics within the partially slipped area when compared to the adjacent area of stable slope. This is most likely a result of the uneven and hummocky terrain in the partially slipped area and its effects on rainfall infiltration, storage and drainage, combined with the displacement-induced jointing present in the underlying sandstone units. The ERT results are used to assess the volume of unstable ground, placing the volume at the upper end of estimates from previous studies. Furthermore, analysis of the ERT dataset for surface displacements shows no movement at the site, which is confirmed by analysis of differential LiDAR plots and ground motion data derived from InSAR. This study demonstrates the application of ERT monitoring on a low activity, high risk slope, highlighting the need to understand subsurface processes at the slope-scale to inform long-term slope management.

Introduction

Electrical Resistivity Tomography (ERT) models provide non-intrusive geoelectrical information related to the spatial distribution of lithological and geotechnical properties in the subsurface [1]. Acquiring repeat resistivity measurements can produce 4D (i.e., time-lapse 2D or 3D) models which reveal how these properties, in particular moisture content, vary spatially and temporally. Recently, ERT monitoring to determine changes in subsurface volumetric properties has gained traction in several areas of geoscience [2]. These include: evaluating agricultural practices (e.g., [3]), understanding plant hydrodynamics (e. g., [4]), assessing the condition of transport infrastructure (e.g., [5]),

identifying groundwater interactions (e.g., [6]), observing geothermal systems (e.g., [7]), determining contaminant concentrations (e.g., [8]), assessing mining waste [9] and monitoring moisture-induced landslides [10].

Wider development of geophysical systems for monitoring landslides has been driven by the demonstrable role that understanding the spatiotemporal characteristics of moisture content and stress plays in warning of impending slope failures at the slope-scale [11]. The sensitivity of resistivity measurements to moisture content complements developments in other geophysical methods for landslide monitoring, such as active seismics to evaluate moisture-induced subsurface stress variations (e.g., [12]) and passive seismics for real-time event detection

---

(e.g., [13]). Using multiple geophysical methods, allied with traditional geotechnical and remote sensing monitoring approaches, can provide a holistic overview of the subsurface hydrological and mechanical conditions preceding slope failure [14]. In recent years, the increase in resistivity monitoring of landslides has been prolific [10], in part due to the development of dedicated resistivity monitoring systems designed to be deployed to unstable slopes (e.g., [15–19]). These systems tend to address unique challenges associated with the deployment of long-term monitoring equipment to unstable slopes, which include: i) difficult access in rugged terrain for equipment installation, maintenance and data retrieval ii) lack of mains power in remote areas, and iii) dynamic slope conditions that threaten the integrity of installed equipment. Autonomous resistivity monitoring systems therefore need to consider these factors in their design, installation, operation and servicing schedules.

One such system is the Proactive Infrastructure Monitoring and Evaluation (PRIME) resistivity monitoring system, designed for the monitoring and assessment of unstable slopes [20]. Through a distributed array of buried electrodes, PRIME autonomously acquires resistivity measurements according to a programmable acquisition schedule. The subsequent time-lapse resistivity models produced from the geoelectrical data can be used to assess the spatial variation in resistivity, and by proxy, relative moisture content of the subsurface over time [21]. Furthermore, estimates of electrode displacements caused by landslide activity can be obtained by inversion of changes in the geoelectrical data [22], giving this geoelectrical monitoring approach motion sensing capability accurate to approximately 10 % of the spacing between electrodes [23].

Understanding moisture content dynamics at the slope-scale is crucial for assessing the stability of landslides. Firstly, increased moisture (typically due to increased rainfall) is a major trigger for landslides around the world [24]). The moisture content of the ground is the primary control on pore water pressure, which combines with the total stresses acting on a potential failure plane to give the effective stress of a soil or weak rock [25]; this effective stress, along with the internal friction angle and cohesive properties of slope material, governs the stability of a slope. In slopes unaffected by destabilising vibrations (i.e., from earthquakes or anthropogenic activity) pore water pressure (dependant on soil moisture content) is the primary dynamic variable controlling slope stability. Secondly, although rainfall thresholds are typically used to predict the occurrence of landslide events, their use tends to ignore the additional complexities of evapotranspiration, infiltration and preferential flow [26]. Soil moisture dynamics for early-warning of failure can be modelled or measured [27]. Measurements tend to be obtained by remotely-sensed [28,29] or sensor-based [30] approaches, but these tend to be limited to periodic, surface-only (or very near-surface) or highly localised measurements respectively. Hence, gaining an understanding of the moisture dynamics of a slope through resistivity monitoring can provide an additional tool to fill the spatial and temporal gaps in the understanding of soil moisture processes operating at the slope-scale.

Here we demonstrate the applicability of resistivity monitoring to assessing and mitigating landslide risk, through the trial of a PRIME resistivity monitoring system deployed on a section of the A40 highway at Leys Bend, located on the border between England and Wales (Fig. 1). We deployed the system on an unstable slope above a major trunk road that crosses several historical landslides. These landslides were unidentified and inactive prior to the construction of the highway in 1964 [31], but during construction two landslides reactivated and damaged the road; one smaller landslide occurred in the inter-carriageway slopes
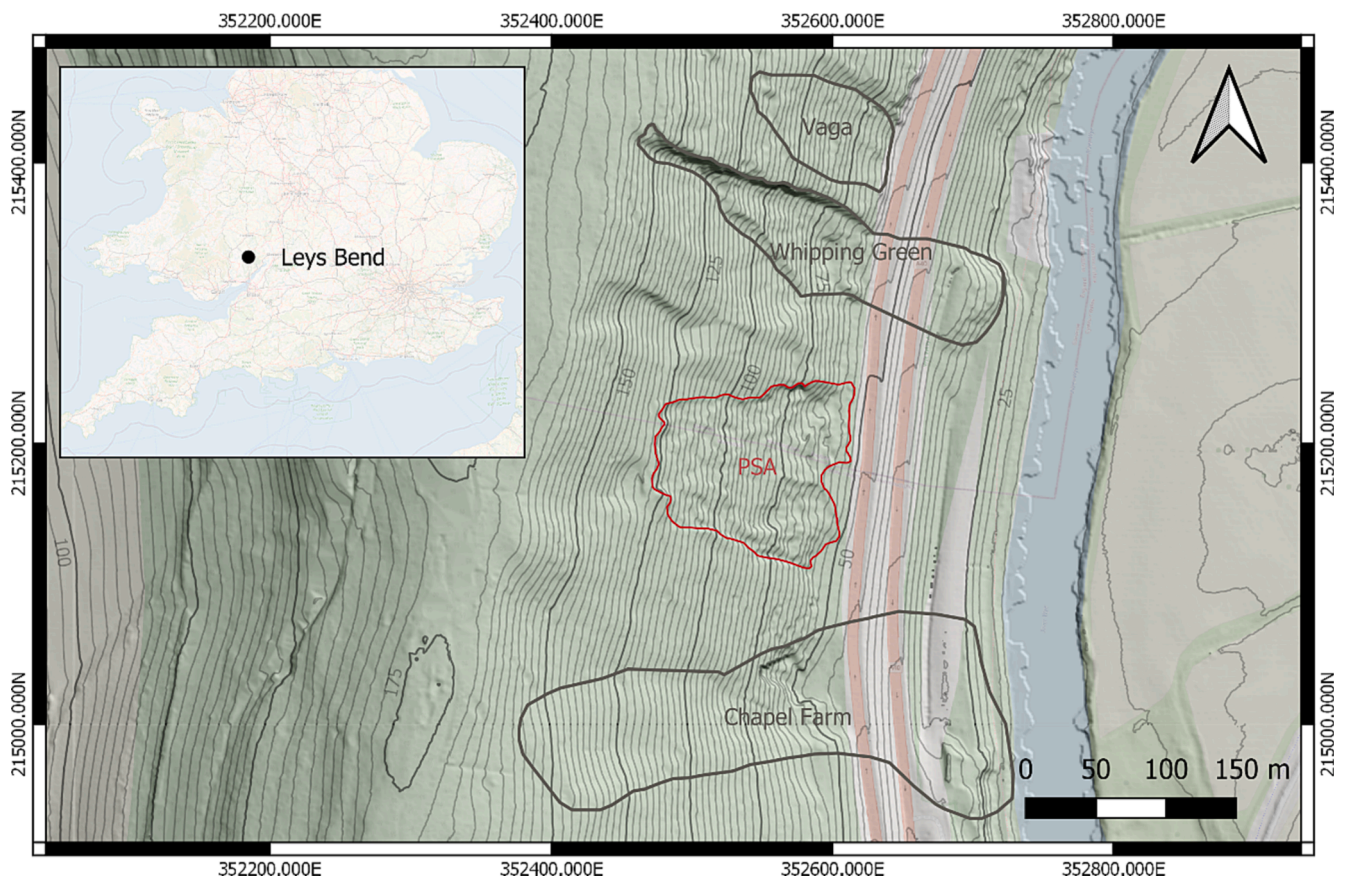

Fig. 1. The location of the 'partially slipped area' (PSA) on the border between Wales and England, and the locations of the landslides initiated by the construction of the A40. The carriageways are shown as pink lines. Contains Department for Environment Food & Rural Affairs material © Crown copyright and database rights [2022]. (For interpretation of the references to colour in this figure legend, the reader is referred to the web version of this article.)

(Whipping Green), and a larger landslide caused the total failure of both carriageways and destruction of farm buildings (Chapel Farm), leading to the redesign and reconstruction of the highway and installation of engineered mitigation measures. The road crossed a further smaller landslide (Vaga) which was not reactivated by the construction works. Loading and slope over-steepening during the highway construction were identified as primary triggers in the reactivation of both landslides, however, at Chapel Farm an intense period of rainfall preceded the dramatic acceleration of the landslide leading to total failure of the highway.

We deployed PRIME to monitor the residual risk posed by an area of slope located above the carriageway that showed partial displacement during highway construction but did not fail, referred to as the "partially slipped area" (PSA). The PSA is located between the Whipping Green and Chapel Farm landslides above the carriageway and has not been subjected to the same loading and over-steepening as the landslides that occurred during construction. Nonetheless, the presence of an area of instability above an (inter)nationally important highway warrants mitigation through cost-effective monitoring, providing the rationale for deployment of a geoelectrical imaging system to monitor the PSA. In this study we present the geoelectrical monitoring results, which we use to i) confirm the site model of the PSA, ii) assess the moisture dynamics of the PSA, and iii) assess the slope displacements from estimates of the electrode movements. We then compare these results with two external sources of movement detection from publicly available LiDAR and InSAR data.

Study area and history

Site description

The study area is a section of the A40 (formally the London to Fishguard Trunk Road) at Leys Bend, located approximately 2.5 km northeast of Monmouth, in Monmouthshire, Wales (Fig. 1). Heading north from Monmouth, the A40 ascends the western flank of a valley bounding the River Wye, crossing the border between Wales and England. The A40 is part of the strategic trunk road network, linking Fishguard in west Wales and London in east England. Of all the roads crossing the border between Wales and England, it has the fourth highest annual average daily flow (AADF) of traffic on the strategic trunk (or 'A') road network crossing the border. Excluding motorways (indicated by the prefix 'M'), it has the second highest AADF of traffic (Fig. 2) of all roads crossing the border. The AADF of the A40 dropped in the mid-2000s (potentially associated with lower levels of traffic on the nearby M4 motorway in the early 2000s, temporarily diverting increased traffic to the A40 until ~ 2003, when the AADF of the M4 increased and the AADF of the A40 decreased) but has been increasing in recent years in line with longer term trends of road use across Monmouthshire, Wales and the wider UK road network. Based on local traffic counts combined with the average hourly patterns of road use across the UK, it is estimated that over 2000 vehicles use the A40 every hour at peak times.

The Leys Bend site comprises the western flank of a valley that bounds the River Wye to the east. The valley hillside extends to over 170 m above sea level, with the River Wye located at ~ 15 m above sea level in the valley floor. The valley side has an average slope angle of ~ 30°. The bedrock comprises the medium-grained sandstones and subordinate beds of mudstones of the Lower Devonian Brownstone Group [31]. Bedding strike is approximately north–south (broadly aligned with the
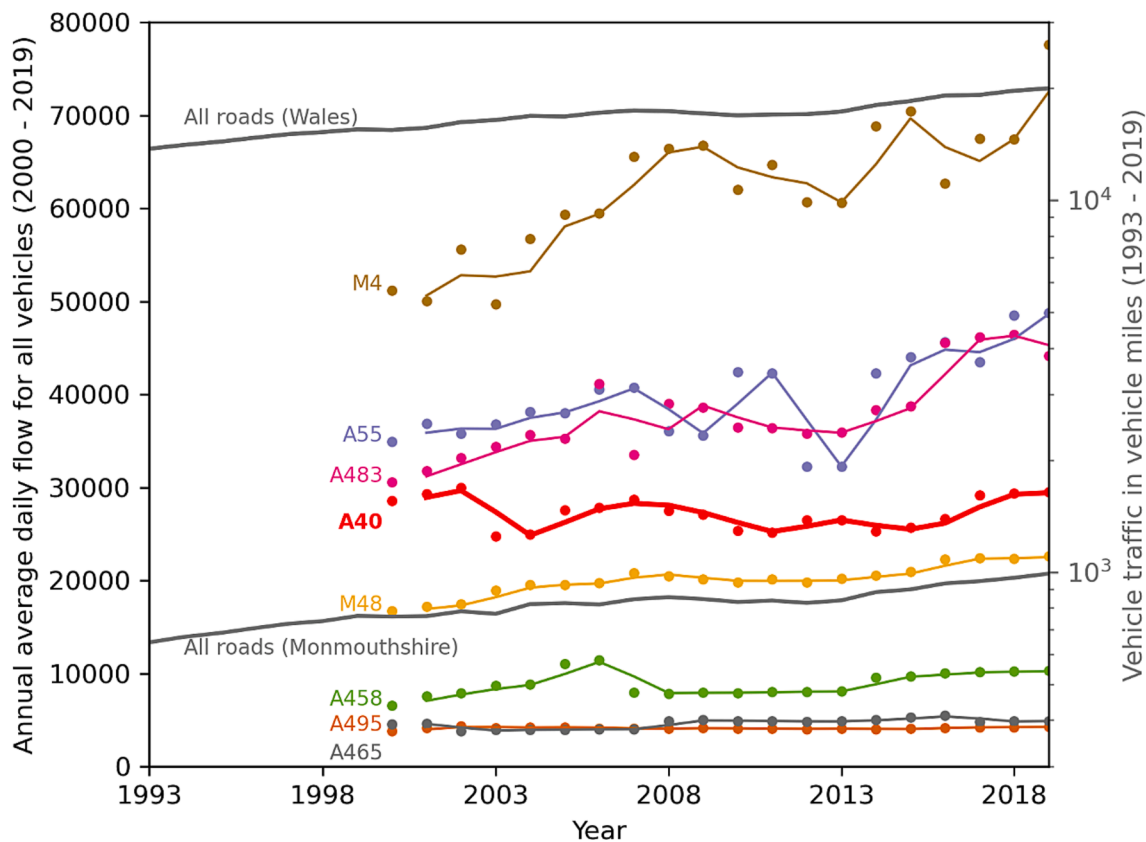

Fig. 2. Road traffic data for roads on the strategic network crossing the border between Wales and England. Annual average daily flow figures (2000–2019) comprise actual and estimated traffic count data from countpoints adjacent to the border. Total vehicle traffic in vehicle miles (i.e., vehicle × miles travelled per year) shown for Monmouthshire and Wales. Contains Department for Transport material © Crown copyright and database rights [2022].

carriageway in this section) and has a consistent dip of 30°. Early and Jordan [31] note that the existing ground surface is largely controlled by the bedding dip, with the exception of the location of the Whipping Green, Chapel Farm and Vaga landslides, where locally deposited bluffs of clay and rock debris exist in various stages of erosion. Significant weathering of the bedrock is observed from the ground surface to 3–6 m below ground level. Smedley et al. [32] observe that the main ground-water table across the hillside ranged between the ground surface and 15 m depth below ground level (with an average depth of 10 m below ground level). However, over half of the installed piezometers were recorded as dry, and significant seasonal variation in groundwater (between 5 m and 10 m below ground level) was observed in boreholes adjacent to the northbound carriageway. These observations, coupled with the jointing of the sandstone and mudstone beds observed by Early and Jordan [31], indicate a complex hydrogeological regime at the site.

Historic landslide failures during road construction

Three ancient landslides are present at the Leys Bend site; the Whipping Green, Chapel Farm and Vaga landslides, named after residences located on the west bank of the River Wye at the base of the slope. Of these, the Whipping Green and Chapel Farm landslides failed during the construction of the A40 dual carriageway in 1964 and 1965, respectively. Early and Jordan [31] provide detailed descriptions of both the geomorphological features of these slides, their movement regimes and associated retention and mitigation works, but a brief summary of their work follows.

The Whipping Green landslide manifested as an area of subsidence in the existing carriageway in April 1964. The slip was remediated, and a gabion wall of rock-filled wire baskets was installed at the foot of the cut to stabilise the carriageway. Slight movements continued in the slope throughout 1964 and following heavy rains at the end of the year, further tension cracks appeared in the carriageway adjacent to the area of prior subsidence. The slip extended above the carriageway, and so a stone wall revetment was installed to prevent this material mobilising on to the road. Furthermore, the previously installed gabion retaining structure was extended to mitigate against further displacements. Later excavations showed a recently developed shear zone extending beneath the gabion wall.

The Chapel Farm landslide showed slight subsidence in May 1964, and the Chapel Farm buildings (after which the landslide was named) were evacuated in September 1964. Small movements continued until December 1964 when a tension crack of several centimetres opened in the embankment slope of the southern carriageway at the same time as tension cracks appeared in the existing road further up the slope. Displacements continued until February 1965 (which was noted as exceptionally dry) before resuming in April 1965. No further significant movements were recorded at the Chapel Farm landslide until the 22nd and 23rd December, when a massive failure occurred, linked to heavy rainfall that occurred between the 16th and 18th of December. This event destroyed the north and southbound carriageway and Chapel Farm buildings lower down the slope.

The A40 construction was completed in 1968 after realigning the road to distribute load in conjunction with the construction of protective earthworks. No record of the cost of the remediation works exists; however, some indication of relative costs can be inferred from a parliamentary debate in 1968, in which the costs of the roadworks at Leys Bend were requested from the Minister for Transport [33]. No specific figures for the cost of roadworks related to remediating the landslides at Leys Bend are provided, instead the costs provided relate to the entirety of work undertaken to upgrade the road to a dual carriageway for a stretch of approximately 6.5 km between Chapel Farm and Goodrich Cross. The original estimate was GBP 1.56 million, the extra cost to the date of the question was GBP 0.56 million, and the total estimated extra cost was GBP 1.09 million, or 70 % of the original estimate. Although it is probable that a significant proportion of this overspend is a result of

landslide damage, it is not possible to know how much of this extra cost is attributable to the remediation of the damaged road.

Ongoing landslide hazard from the PSA

A legacy of the A40 construction at Leys Bend was the identification of the PSA, which sits between the Whipping Green and Chapel Farm landslides. The PSA has a slope angle of approximately 28°, is approximately 130 m wide and extends 130 m upslope, with the toe of the PSA sitting approximately 20 m above the northbound carriageway [32]. Early and Jordan [31] identified this area as having partially slipped by shear failure of the mudstone beds and comprising a mosaic of slipped units (i.e., units separated by fractures), experiencing differential displacements from < 1 to 145 m. The average depth of slip was estimated at between 2 and 5 m below ground level, and up to 6 m below ground level in some areas. The PSA has an area of 1.35×10^6 m^2 determined from LiDAR data acquired in 2020 (Fig. 3), giving lower and upper range of volume between 2.7 and 6.75×10^6 m^3, based on the average depth to the slip surface observed by Early and Jordan [31].

Several reasons for the limited displacement observed in the PSA were proposed by Early and Jordan [31], including, i) a lack of 'free edge' formation in a failure wedge due to the geological strike position relative to the slope angle, ii) lateral support at the bounds of the PSA, iii) thinner and less persistent mudstone beds, iv) free drainage promoted by the fractured slip mosaic, v) afforestation and vi) sandstone scree formation inhibiting movement. However, despite proposing these mechanisms of stabilisation, Early and Jordan [31] also clearly identify the PSA as posing a risk to the A40, despite the lack of movement observed in the PSA between the remediation of the A40 and the publication of their work. In a more recent study, Smedley et al. [32] observed that the toe berm installed as part of the A40 construction beneath the PSA would mitigate against future deep seated failures of the PSA. However, they acknowledged the potential hazard posed by slip surfaces that daylight above the A40, which could mobilise smaller volumes of material on to the carriageway. Such a failure could still pose a risk to road user safety and cause significant economic impacts in road closure and clean-up costs.

Methodology and data

PRIME system design and installation

The PRIME system comprises an array of distributed electrodes connected to a central unit by strengthened cables, typically buried in the near-surface (10–30 cm depth). Electrodes are inserted in to the subsurface at a consistent spacing along a profile, typically installed with a conductive fill material to ensure good electrical contact with the ground (indicated by low measured contact resistance). Geoelectrical measurements, each of which utilises four electrodes, are made across the deployed electrode array at pre-defined spatial intervals, allowing the recovery of the 2D distribution (in cross-section) of the resistivity beneath the profile. The time to acquire a full set of measurements scales with number of electrodes deployed per system, but at maximum electrode capacity, these are typically complete within two hours, allowing the system to make several sets of measurements per day if required. PRIME is designed with low power requirements (10 W), and can be operated using locally installed solar or wind power sources. Wireless telemetry facilitates control of the unit from a remote (office) location, while state of health information and acquired resistivity data can be inspected and retrieved via the same connection.

We installed the system on the PSA at Leys Bend in June 2017 as part of a trial monitoring period in conjunction with National Highways, the UK government-owned company responsible for operating and maintaining the major highway network in England (Fig. 3). The aim of the trial was to monitor resistivity changes driven by subsurface moisture content variation. Increased moisture content (linked to increased rainfall) played a role in the acceleration of the Chapel Farm landslide in
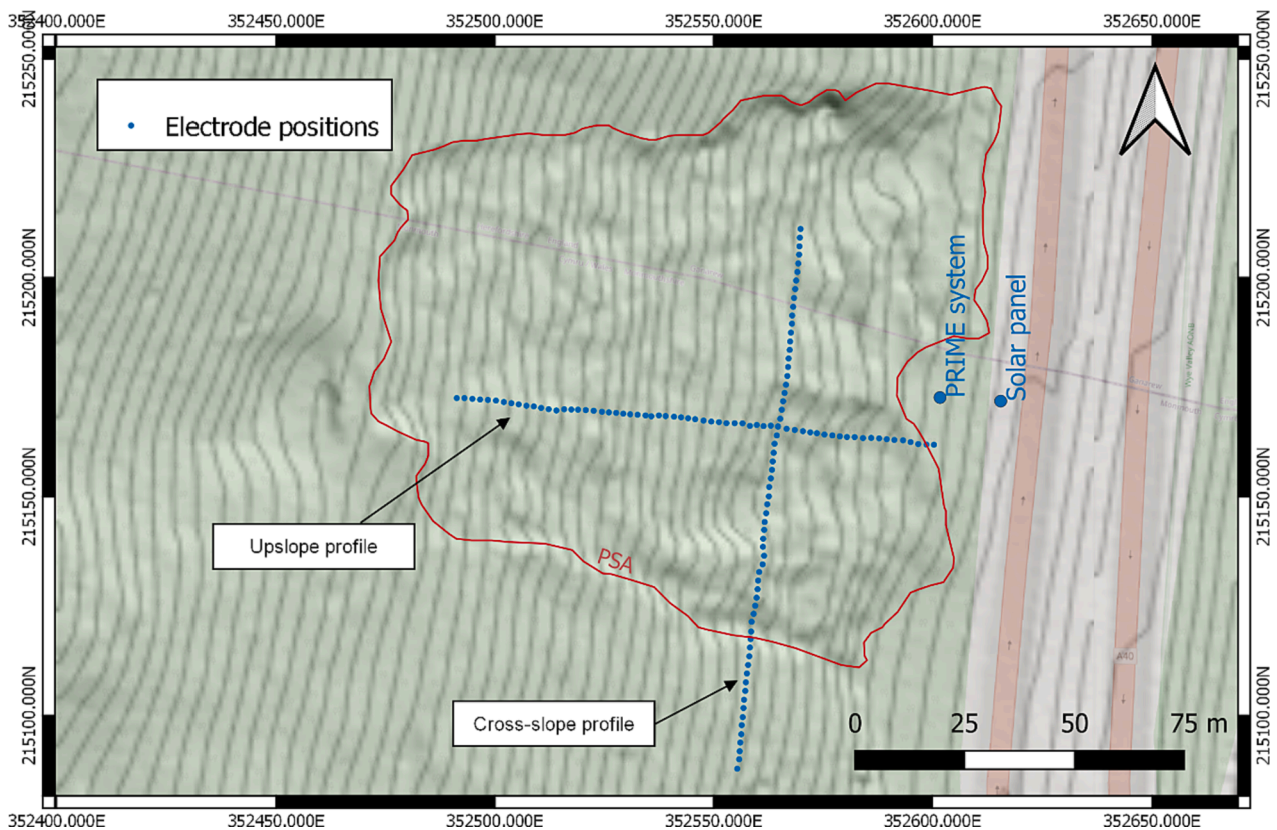
Fig. 3. Location of the PRIME ERT system deployed to the PSA at Leys Bend, comprising the main PRIME unit, electrode locations, and solar panel. The carriageways are shown as pink lines. Contains Department for Environment Food & Rural Affairs material © Crown copyright and database rights [2022]. (For interpretation of the references to colour in this figure legend, the reader is referred to the web version of this article.)

December 1965, accelerating displacement from limited subsidence to catastrophic failure. Although the PSA has not been impacted by loading and over-steepening in the same way, the existence of a weakened mass above a major strategic road warrants ongoing monitoring. The PSA presented challenging terrain for equipment installation, including the steep slope, a thick cover of granular scree and leaf litter overlying shallow bedrock, and restricted access to the site along the northern carriageway of the A40 (Fig. 4).

We installed two linear electrode arrays on the slope, centred on the lower part of the PSA (Fig. 3). We deployed the arrays orthogonally to each other, with one profile deployed parallel to the direction of slope (the upslope profile; Fig. 4a) and one deployed perpendicular to the slope direction (the cross-slope profile; Fig. 4d). Along each profile, we installed 64 electrodes at 2 m separations, totalling 128 electrodes in the deployment. The cables connecting the electrodes to the PRIME system could not be buried due to shallow bedrock and loose ground cover; instead we wrapped the cables with protective sheathing to minimise damage from animals (Fig. 4). We used a total station to position and record the locations of electrodes (dense vegetation prevented the use of a GNSS system for surveying). To overcome poor electrical contact with the granular scree and leaf litter cover, we used long (~30 cm) electrodes. Where contact resistances were high, we installed the electrodes in hand-augered holes which we backfilled with an electrically conductive granular material; prior attempts to fill the holes at these locations with a bentonite slurry resulted in the escape of bentonite into the underlying sandstone joints in several areas.

We installed a solar panel adjacent to the A40 to power the PRIME system, away from the tree cover (Fig. 4e). After installation of the electrode arrays and solar panel, we tested the system to ensure good contact resistance between the electrodes and the ground. The first measurement set with sufficient data quality was retrieved on 21/07/

2017. This baseline dataset forms the reference point against which we calculate relative changes in resistivity until the conclusion of the monitoring period on the 09/02/2019. Being able to access the system remotely minimised the need for site visits to retrieve data, thus reducing the risk to personnel accessing the site along the A40 highway.

The system was scheduled to acquire one full set of forward and reverse (i.e., normal and reciprocal) readings per week using a dipole–dipole array with dipole lengths $a = 1$–6 electrode spacings and dipole separations na with $n = 1$–8, totalling 1980 measurements on each line. In total, 62 datasets (including the baseline dataset) were acquired in the 81 weeks that the system was operational. There were some data collection gaps concentrated over the winter of 2017–2018, comprising: i) mid-September to the start of October 2017, ii) mid-October to mid-November 2017, iii) mid-November to mid-December 2017, iv) start of January to end of January 2018, and v) mid-February to beginning of April 2018. From this final date onward, the system acquired data every week, as per the design schedule.

We used temperature data from a weather station located 7.2 km to the west of the site (Station IGWENTMO3, [34]) to calculate the daily average air temperature from the maximum and minimum recorded daily temperatures. We also used the rainfall recorded at the same station for comparison with the resistivity data for the monitoring period. Furthermore, we use this data to calculate effective rainfall for the site. Effective rainfall equals the difference between precipitation and modelled evapotranspiration, based on air temperature, incoming solar radiation and the global position of the site, along with an estimate of the influence of local vegetation according to Hargreaves and Samani [35] and Samani [36]. Consequently, effective rainfall can be positive during periods of increased precipitation with low evapotranspiration or negative when evapotranspiration exceeds input from precipitation. Decreases in resistivity are generally associated with periods of positive

Fig. 4. Photos from the Leys Bend site showing a) upslope profile (looking west), b) blocks bounding the eastern flank of the PSA (looking west), c) steep gradient of the slope (looking south), d) cross-slope profile (looking north), and e) the PRIME cabinet and solar panel (looking north east).

effective rainfall (i.e., net moisture gain), whereas resistivity increases are associated with periods of lower moisture (i.e., net moisture loss), although the lag times between these above-ground conditions and their manifestation in the subsurface are complex and highly site specific, and dependent on local infiltration conditions [37]. Despite this, studies have shown that generally good correlations exist between estimates of effective rainfall, direct moisture measurements, and other geophysical proxies (e.g., [12]).

At the time of the system deployment, we installed local temperature sensors at depths of 0.1, 0.3 and 0.68 m below ground level (bgl). We use this data to correct the resistivities for seasonal temperature changes as described in the section below.

PRIME data processing

Resistivity data processing

During the monitoring period, 62 complete weekly datasets were recorded. We processed this data using standard processing steps including raw data assessment and filtering to remove unreliable data, 4D inversion to derive the resistivity distribution and change within the subsurface below the profile lines and temperature correction to remove the effect of seasonal temperature changes in the resistivity timeseries.

The data quality assessment was done based on reciprocal errors, which are derived from forward and reverse measurement pairs and provide a well-established way to quantify measurement errors [38,39]. Overall, reciprocal errors were higher during the dry summer months due to an increase in contact resistances. Furthermore, we identified five electrodes that showed consistently high contact resistances and poor data quality, indicating that they were either completely disconnected or placed in loose ground. During filtering, we deleted all data involving the five problematic electrodes and applied filter thresholds removing all data with i) reciprocal errors higher than 5 %, ii) contact resistances higher than 10,000 Ω and iii) negative voltages. After filtering, on average, 78 % of data remained during the wet period. During the dry period, the amount of remaining data was marginally lower at 76 %. For the inversion, the removed data were interpolated and down weighted by assigning a large error to the interpolated value as in Wilkinson et al. [40].

During data inversion, the resistivity distribution and its change over time is derived by iteratively minimizing the difference between measured and modelled data[41]. This was done for each profile line separately with the software *Res3DInvX64* (Geotomo Software/Seequent). This software applies a full 4D smoothness constrained least squares inversion algorithm, which inverts all time-steps simultaneously in 3D space [40]. Even though the profiles are approximately 2D lines, we favor a 3D inversion in space as this provides better results where offline changes in resistivity and topography may exist [15]. In order to stabilise the non-unique and ill-posed inversion problem, the software applies smoothness constraints both in the spatial and temporal dimensions. Since we expect smooth changes of resistivity in space and over the weekly time steps, we used L2-norm smoothness constraints for both dimensions. Furthermore, we used L1-norm on the data misfit making the inversion more robust to the relatively noisy data.

To avoid overfitting of noise during the inversion process, it is important to weight the data with an appropriate error estimation. In this study we applied the approach suggested by Lesparre et al. [42], where a separate error model is created for every time step by binning the reciprocal errors as a function of transfer resistance and fitting a quadratic model through each respective bin average shifted-up by two times the bin standard deviations. This results in an envelope fit where the error model encompasses ∼ 95 % of the data errors and where the error estimates represent the reciprocal error distribution at every time step[40]. In addition, the contribution of numerical modelling error was incorporated by adding a constant fraction (2 %) of the measured transfer resistance[43]. With these settings, the inversion process obtained a good fit with an average absolute data discrepancy of 5.9 % for

the upslope profile and 11.9 % for the cross-slope profile.

Seasonal variations in temperature can cause electrical resistivity changes in the same order of magnitude as expected by the target hydrological processes[44,45]. To remove the unwanted influence of seasonal temperature, we corrected the resistivities to a standard temperature of 20 °C. For this, we used the temperature time-series measured at 0.0, 0.1, 0.3 and 0.68 m depth to fit a simplified seasonal temperature model allowing the subsurface temperatures to be estimated at every time step as described in Brunet et al. [46] and [37]. These temperature estimates are then used to adjust the model resistivities to the standard temperature using the ratio model suggested by Hayashi [47] and applying a correction of −2 % per °C temperature deviation [48]. From the final resistivity models at every time step, we calculated percentage change in resistivity with respect to the chosen reference date (21/07/2017).

Resistivity changes due to electrode movement

Time-lapse changes in the measured transfer resistances depend not only on variations in the subsurface resistivity distribution in the vicinity of the electrode arrays but also on changes in the relative positions of the electrodes that can occur on unstable slopes[22,23,49]. We used the inverse method described in Wilkinson et al. [49] to assess whether any signatures characteristic of movement were present in data from the upslope array. We applied the method to data measured on similar dates in subsequent years (on 07/02/2018 and 09/02/2019) with $a = 2$ m and $n = 2$–3, $n = 1$–3 and $n = 1$–4, applying weak, moderate and strong constraints on the sum of the total movement and of the uphill movement.

Results

Baseline characterisation results

The initial baseline model was produced from data acquired on 21/07/2017 (Fig. 5). Both arrays are centred in the PSA, with the exception of the southernmost 30 m of the cross-slope profile, which is located upon a stable part of the slope outside of the PSA. The surface layer (i.e., top 5 m bgl) shows the greatest heterogeneity in resistivity, displaying various sized zones of resistivity with sharp boundaries comprising both high (>3,000 Ωm) and low (<200 Ωm) resistivity. When comparing the upslope profile to the conceptual schematic slope model proposed by Smedley et al. [32], the competent bedrock underlying the PSA (i.e., at depths>5 m bgl) shows a more confined range of resistivity values (<300 Ωm) with smoother transitions in resistivity values across the profile (Fig. 5a). Above this lower layer, there is a layer of heterogeneous resistivity (generally showing resistivity values of > 300 Ωm) between 0 and 5 m bgl, with the depth extents of this heterogeneous surface layer corresponding with the base of the weathered rock forming the PSA, giving some further detail on the depth to the base of the PSA along the slope. The Comparison with the schematic model of Smedley et al. [32] suggests that the upslope profile should be sited completely within natural rock, with only a very small wedge of surface gravel potentially present at the base of the section. This gravel was not observed during the system installation, but if this gravel is present, it either does not have a significant effect on the character of the resistivity in this area or is not associated with sufficient contrast in resistivity with the underlying material to be detectable.

The near-surface heterogeneity in resistivity is present in both ERT profiles (Fig. 5b). On the upslope profile, low resistivity (<200 Ωm) zones are located between 0 and 10 m and 13–19 m horizontal distance (from the west of the profile), with high resistivity (>3000 Ωm) zones located between 19 and 23 m, 29–37 m and 56–71 m horizontal distance. On the cross-slope profile, the initial 30 m of the profile (from the south) is located on the stable part of the slope, and shows a surface layer of high resistivity (>3000 Ωm) extending until the break of the slope
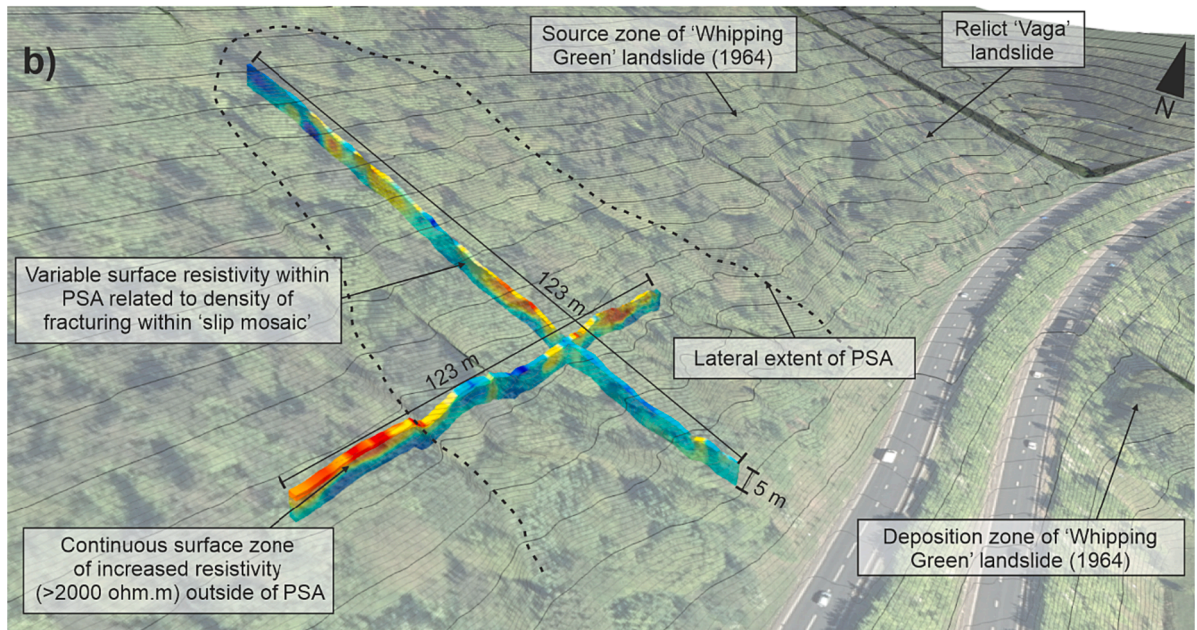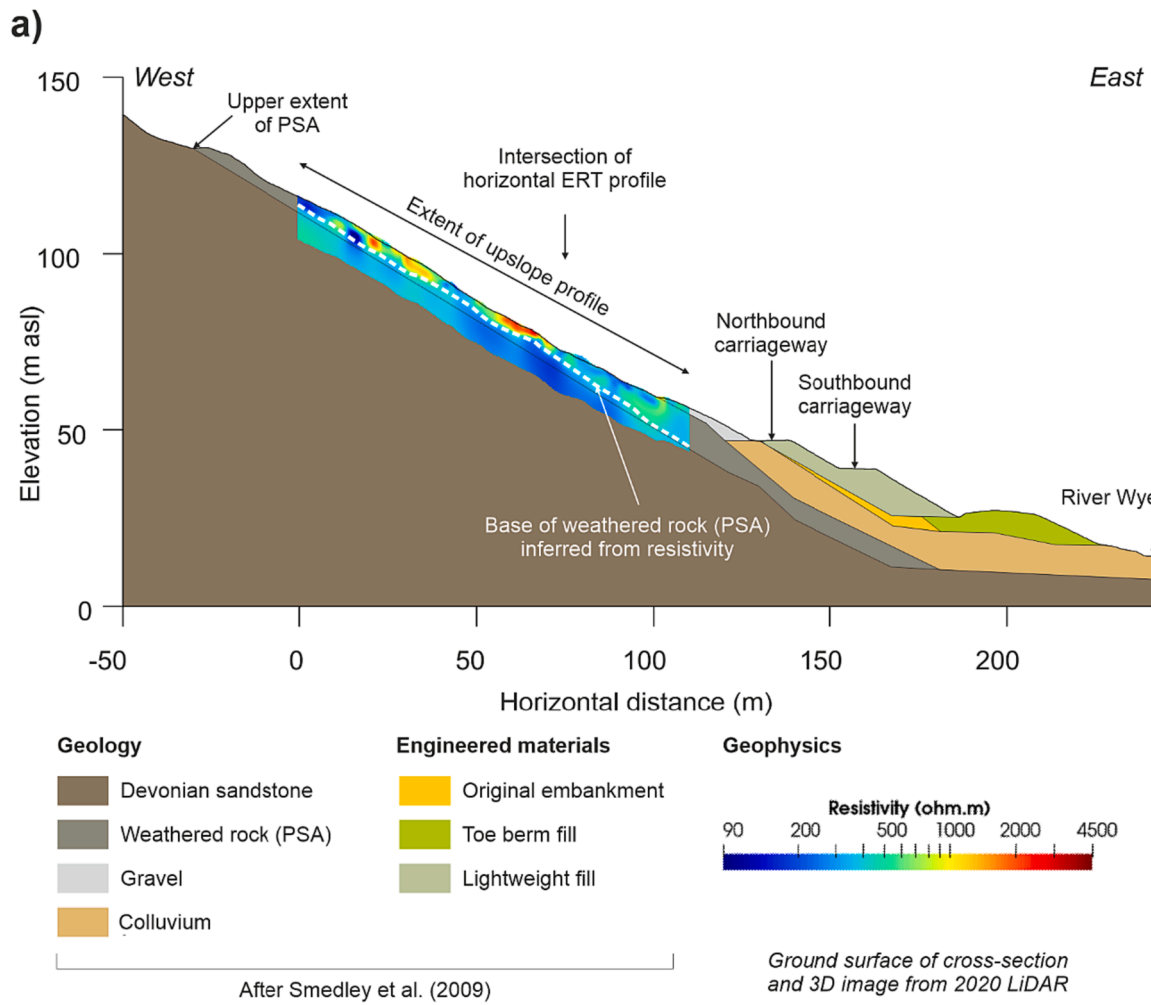
Fig. 5. Views of the initial baseline resistivity models from Leys Bend acquired on 21/07/2017, showing a) the upslope profile overlain on to a schematic cross-section (after [32], and b) 3D view of the site showing the top 5 m of both profiles, with 5 m topographic contours (dark lines) and 0.5 m topographic contours (light lines) shown. Contains Department for Environment Food & Rural Affairs material © Crown copyright and database rights [2022]. Contains Getmapping materials © Getmapping Plc [2022].

that marks the southernmost extent of the PSA. From 30 to 70 m horizontal distance, the surface layer mostly shows lower resistivity values, and from the point of intersection with the upslope profile at 79 m horizontal distance to the northern extent of the profile, the surface layer shows mostly zones of high (>1000 Ωm) resistivity.

Time-lapse resistivity monitoring results

Changes in resistivity are calculated as percentages relative to the baseline survey (t0) collected on 21/07/2017 (Fig. 6). Of the additional 61 datasets (i.e., time-steps) collected, eleven are displayed, from times with approximately equal spacing throughout the monitoring time-series. Results of time-lapse resistivity images are compared with modelled effective rainfall (Fig. 7), as there are no soil moisture sensors installed at the Leys Bend site.

The PRIME system was installed during a relatively dry period in the (UK) summer (July 2017), at a time showing moderate negative effective rainfall (Fig. 7). Effective rainfall remains negative at the next time-step t07 (t0 + 52d) at the beginning of autumn (September 2017). Effective rainfall becomes positive by late autumn (October 2017) and remains positive through winter (until January 2018), with t10 (t0 + 120d) and t13 (t0 + 154d) showing decreases in resistivity at the surface, with deeper extents in t13 than t10. In late winter by t18 (t0 + 207d), despite the marginal fluctuating positive and negative effective rainfall throughout the first half of February 2018, there have been significant decreases in resistivity across the majority of both profiles, indicative of the sustained levels of positive effective rainfall leading up to February 2018. The decreases in resistivity generally extend to the base of both profiles, with the exception of the southernmost part of the cross-slope line (located outside of the PSA), and some other discrete zones along the cross-slope profile, which show either no change, or increases in resistivity. These include the surface area located between 55 and 68 m horizontal distance (associated with a local topographic high in the profile) and at the deeper part of the profile between 80 m horizontal distance and the northernmost extent of the cross-slope profile. It is notable that these three specific locations along the cross-slope profile never show decreases in resistivity relative to t0 across the entire time-series.

Despite a return to consistent positive effective rainfall values by t20 (t0 + 259d) in spring (April 2018), resistivity remains much lower than at t0 and shows a general decrease in resistivity values from those observed in t18. However, very little change in resistivity is observed between t20 and t27 (t0 + 309d) at the end of spring (May 2018) despite a shift from general positive to negative effective rainfall throughout the end of spring. This indicates a potential lag effect between the onset of changes from positive to negative effective rainfall and changes in subsurface resistivity, as at one year after installation in summer (July 2018), t35 (t0 + 365) there is a reverse in the decreasing resistivity trend. In t35, many sections of both profiles showing increases in resistivity, with the exception of localised surface areas at the southernmost end of the cross-slope profile, and halfway along the upslope profile. This trend in resistivity increase continues to t41 (t0 + 412d) at the end of summer, which marks the end of a long period of extreme negative effective rainfall between the start of June and end of August 2018. This time represents the driest period in the entire monitoring time-series (based on the effective rainfall data).

Little change in resistivity is observed in autumn between t41 and t48 (t0 + 461d), which encompasses a period of fluctuating positive and negative effective rainfall between the start of October and end of November 2018. This period experiences generally low effective rainfall levels punctuated by isolated events of extremely high effective rainfall, however, by winter (December 2018), effective rainfall shows some of the highest sustained levels across the monitoring time-series, and a corresponding dramatic decrease in the resistivity of the surface layers of both profiles is observed in t56 (t0 + 518d). Effective rainfall levels remain positive or only marginally negative throughout winter until the

end of the monitoring time-series in February 2019, with the final model at t61 (t0 + 568d) showing a similar resistivity change distribution to that observed in t56.

Motion detection from electrode displacement results

Applying the inverse method of Wilkinson et al. [49] revealed no clear signatures characteristic of electrode movement. Any potential indications were strongly dependent on the magnitude of the damping constraints, and predominantly occurred in the vicinity of the electrodes with poor data quality that had been removed from the resistivity inversion. Therefore, we interpret these as artefacts rather than true estimates of movement. Only one persistent displacement estimate was produced from the various combinations of data and constraints, which was for the electrode at the intersection of the upslope and cross-slope lines. We note that strong localised resistivity changes occur in the near surface of the geoelectrical models at this intersection (Fig. 5), and that these changes occur consistently on both lines (strongly suggesting that they are not an artefact of electrode movement on the upslope line). Therefore, we also interpret the apparent displacement of the electrode at the intersection as an artefact, caused by the movement inversion trying to fit to a highly localised ground resistivity change. Therefore, we conclude that no electrode motion occurred during the monitoring period at Leys Bend.

Discussion

Landslide characterisation and monitoring using resistivity

The baseline resistivity model (Fig. 5) confirms the depth to the base of the PSA as assumed in the conceptual slope profile of the site proposed by Smedley et al. [32]. The depth of the PSA is relatively consistent along the length of the upslope profile, located at 4 m bgl (± ~0.5 m). In the cross-slope profile, the depth to the base of the PSA is marginally shallower, located at ~ 3.5 m bgl, and displays some shallowing to the north. Based on these depths and using the area of the PSA identified in the 2020 LiDAR data (Fig. 3), the volume of the PSA can be refined from estimates of 2.7–6.75 × 10^6 m^3 (based on depth estimates by [31] to being closer to 4.72–6.07 × 10^6 m^3 using the range of depths observed in the baseline resistivity model.

However, the baseline resistivity model also shows significant spatial variation in resistivity within the surface layer of the PSA (Fig. 5). In the baseline model, there are three zones of increased resistivity values in the surface layer (>3000 Ωm) located at 56–71 m horizontal distance on the upslope profile, and 0–30 m horizontal distance and 79–124 m horizontal distance on the cross-slope profile. These areas continue to display increased resistivity values compared to the rest of the model throughout the time-series (Fig. 6) and when averaged across the time-series (Fig. 8a). Zones of high resistivity also tend to show the greatest standard deviation across the time-series (Fig. 8b), suggesting their resistivity varies the greatest, which is demonstrated when considering the minima in change of resistivity (Fig. 8c) and maxima in change of resistivity across the time-series (Fig. 8d). These temporal statistics are a useful means of identifying spatial regions of geophysical time-series that show different lithological and hydrological properties (e.g., [12]).

In summary, areas with areas with low resistivity in the baseline model (Fig. 5b) coincide with low standard deviation (Fig. 8b), thus consistently remaining at relatively low resistivity throughout the monitoring period. The opposite is true for areas of high resistivity in the baseline model (Fig. 5b), which tend to coincide with areas of high standard deviation across the time-series (Fig. 8b) indicating greater changes in resistivity in these areas. In the area of stable slope (which shows higher average resistivity across the time-series) the surface layer shows periods of decreased resistivity in response to periods of increased effective rainfall, especially in the winter months. The lower layer in this area shows some periods of lowered resistivity, although it never
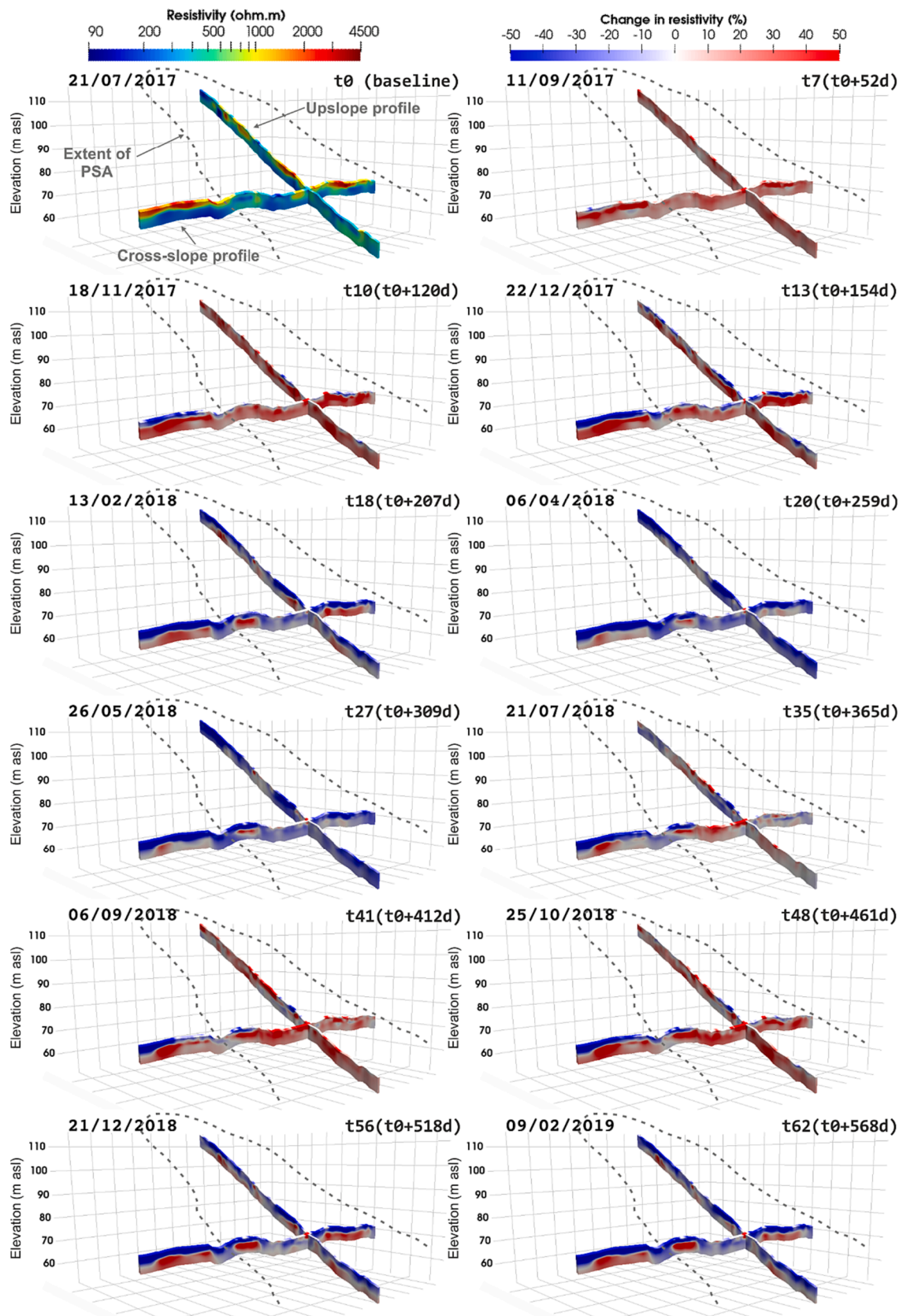
Fig. 6. Time-lapse resistivity models from the Leys Bend site. Top left (21/07/2017) shows the baseline image against which subsequent changes in resistivity are calculated.
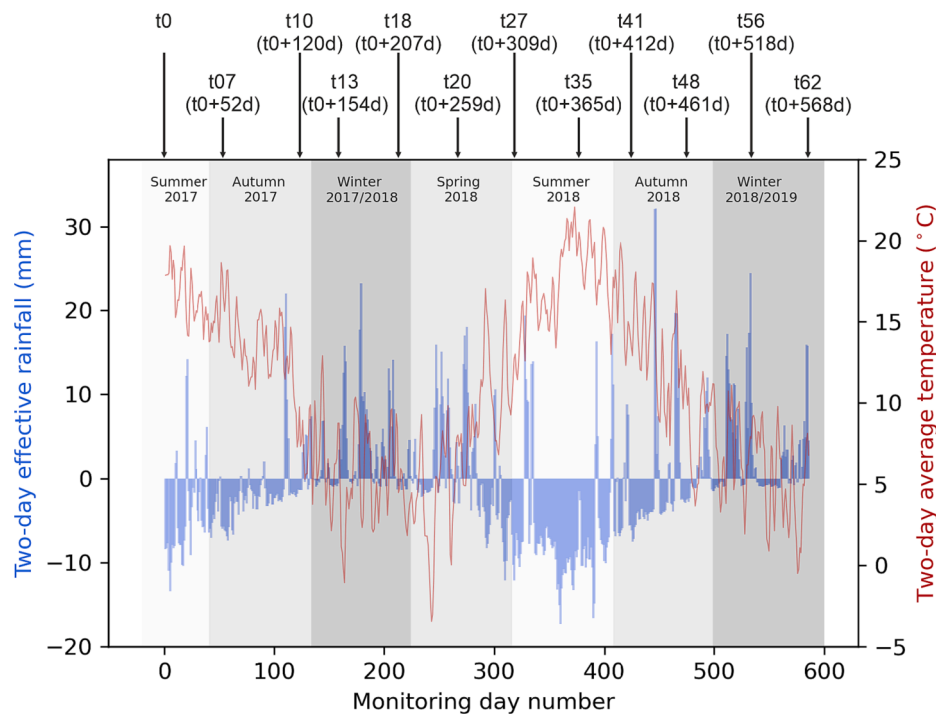
Fig. 7. The two-day effective rainfall (blue) and two-day average temperature (red) for the monitoring period, with the times of the models shown in Fig. 6 indicated. Shaded regions show meteorological seasons, comprising summer (June – August), autumn (September – November), winter (December – February) and spring (March – May). Data sourced from Station IGWENTMO3 [34]. (For interpretation of the references to colour in this figure legend, the reader is referred to the web version of this article.)

decreases below the value of the baseline model, suggesting there may have been some increased moisture stored in this layer during installation. In the PSA, the relationship between effective rainfall and the relative increase and decrease of resistivity in the surface and lower layers is less pronounced, with some areas showing stark decreases in resistivity in both the surface and lower layers in response to rainfall, and with other areas showing characteristics more similar to the stable slope (i.e., rapidly decreasing resistivity in the surface layer in response to rainfall, with only moderate decreases at depth). The complex patterns of differential infiltration and responses to rainfall shown by the time-lapse resistivity results is likely caused by a combination of factors, including i) the variable slope angle and hummocky terrain of the PSA, which unlike the more uniform slope seen outside the PSA (Fig. 3) will impact localised runoff and infiltration rates as well as subsurface storage and drainage through rock layers, and ii) the complex nature of the slip mosaic within the PSA, which Early and Jordan [31] note comprise sandstone in various degrees of disturbance, with the slip mosaic defined by jointing. These differential sizes in joint sets will have a significant impact on both the bulk resistivity of the subsurface, and also the ability of water to be transmitted through and stored within the ground.

Comparison of deformation measurements to assess the hazard posed by the PSA

Early and Jordan [31] observed no displacement of the PSA between the completion of remediation of the A40 in 1968 and the publication of their work. More recently, Smedley et al. [32] compared airborne LiDAR data acquired in 2005 with the original topographic survey acquired by Early and Jordan [31] from stereoscopic imagery acquired in 1964. Smedley et al. [32] noted that the lateral extents of the PSA remained broadly unchanged, with the exception of a potential increase in height of the backscarp and potentially more 'hummocky' terrain, which may be associated with differences in resolution between the two survey methods. In this study, analysis of possible electrode displacements

determined by movement inversion indicate that there has been little to no movement across the monitoring array. This is corroborated by two external data sources: i) differential analysis of LiDAR from data acquired in 2006 and 2020 (i.e., pre- and post-PRIME resistivity monitoring), and ii) the European Ground Motion Service (EGMS) database.

Two composite LiDAR datasets from 2006 and 2020 (both acquired at 2 m horizontal resolution with vegetation removed) were analysed to detect topographic variations in the PSA. The 2006 data were subtracted from the 2020 data, and a colour shaded overlay showing variations of ± 1 m draped over the 2020 hill shaded data (Fig. 9). The differential LiDAR shows several zones of accumulation (blue) toward the base of the PSA, and to a lesser extent the flanks and localised area of the top of the PSA. Some localised areas of depletion (red) are also located in the centre of the PSA and at the flanks, although these are smaller in both size and amplitude than the areas of accumulation. Generally, the differential LiDAR values across the majority of surface of the PSA do not show any major contrast to the areas of slope outside of the PSA. This suggests that the PSA has not deformed significantly in the period 2006 to 2020, with the exception of the highly localised zones identified above.

The EGMS database provides measurements of ground motion derived from interferometric synthetic aperture radar (InSAR) measurements. InSAR has been increasingly used to measure ground deformations in recent years, and has allowed for the remote observation of landslide hazards with unprecedented temporal resolution across the world [50]. However, accurate and repeatable InSAR measurements typically rely on the existence of persistent scatterers (i.e., points on the ground that sufficiently reflect the satellite signal); where persistent scatterers are not present, InSAR measurements can be significantly improved with the installation of corner reflectors (e.g., [51]). Although the vegetation cover across the slope of the PSA prevents the installation of corner reflectors, there are two EGMS points close to the PSA, located on the A40 (Fig. 9). Data from each EGMS point shows measurements of vertical ground deformation, with a corresponding linear trend line indicating the average trend of deformation (Fig. 10). EGMS point
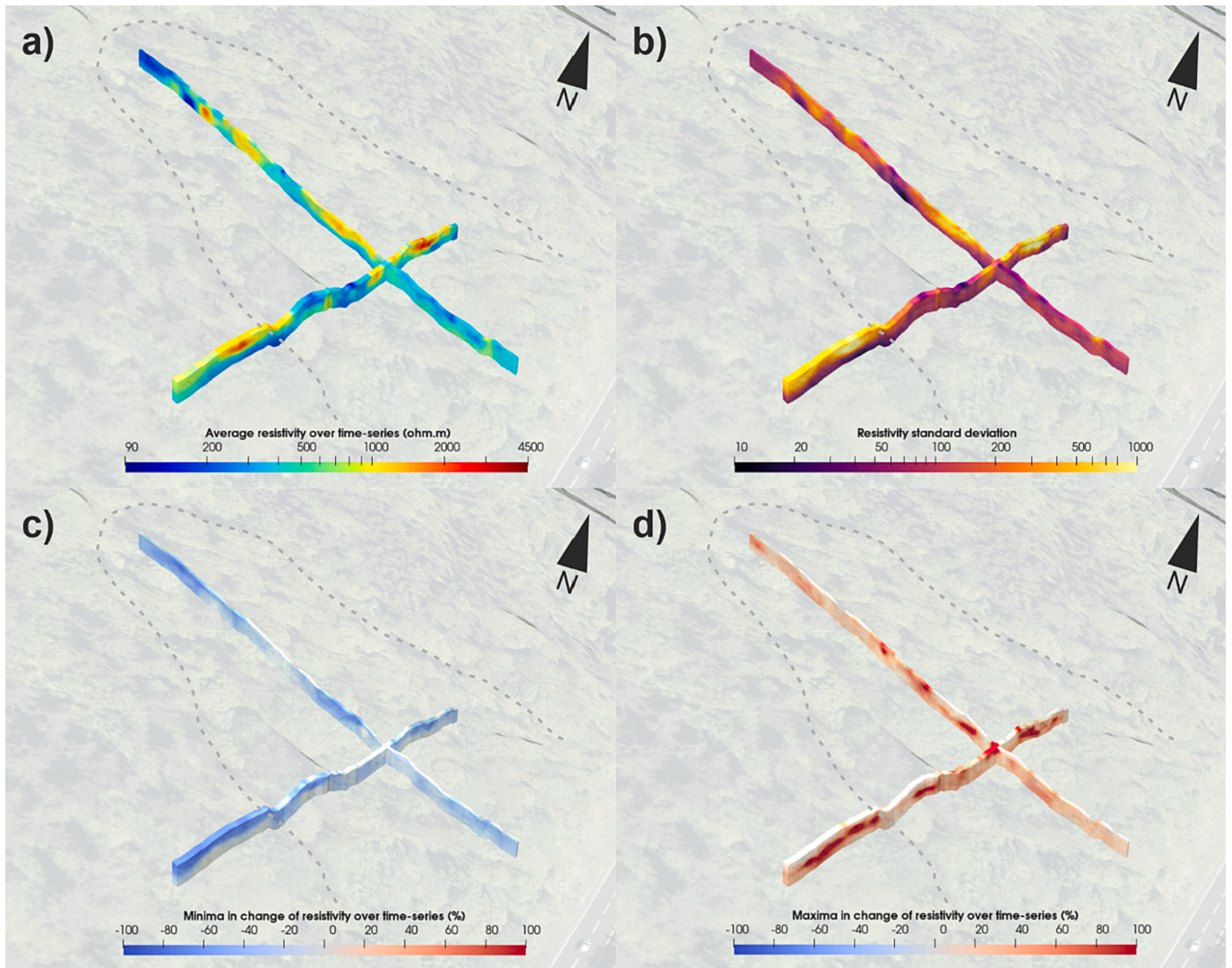
Fig. 8. 3D views showing a) the average resistivity across the time-series and b) the standard deviation of resistivity across the time-series, c) the minima in change of resistivity change across the time-series, and d) the maxima in change of resistivity across the time-series. Contains Department for Environment Food & Rural Affairs material © Crown copyright and database rights [2022]. Contains Getmapping materials © Getmapping Plc [2022].

40dqea9gyg, located 38 m beneath the PSA, shows a total average of −10 mm vertical displacement between 11/01/2016 and 21/12/2020, equating to an average of −2 mm/year vertical deformation (RMSE = 1.8 mm). Point 40dqjGowAk, located 115 m north-northwest of the PSA, shows a similar level of total displacement for the same period: −9mm vertical displacement, averaging −1.8 mm/year (RMSE = 3.6 mm). Two limitations of the EGMS data are the precise location and measurement density of the points; the point locations indicated can vary over several metres, and measurements are taken within a 20 m × 5 m cell around these locations. However, given the bounding of the A40 road surface to the east and west by vegetation (which would prevent signal reflection), it is highly probable that the observably coherent signal measured at the two EGMS points is returning from the surface of the A40. The RMSE for EGMS point 40dqjGowAk (located further from the PSA) shows much higher noise levels; nonetheless, the rate of vertical displacement for both points is minimal and consistent, suggesting no impact of accelerated deformation on the A40 road surface immediately beneath the PSA. The rates of vertical displacement of both of these points are similar to rates of vertical displacement observed in nearby points away from the Leys Bend site. Therefore, based on the assessment of both differential LiDAR and data from the EGMS, the PSA can be characterised as a low activity hazard.

Monitoring of low activity hazards posing high risk to infrastructure

Landslide hazards in the UK are generally perceived as low risk [52]. At Leys Bend, the immediate hazard posed by the PSA appears to be low, based on the absence of significant slope deformation suggested by the analysis of data from several sources, including the PRIME system, InSAR and LiDAR measurements. Historic studies indicate this has been the case for over 50 years [31,32]. However, the impact of a landslide on the A40 is demonstrated by the Whipping Green and Chapel Farm landslides that occurred during construction of the A40, resulting in significant remediation works, road redesign, installation of mitigation measures and likely contribution to a significant overspend in the construction of the A40 in this section. In a modern-day context, the financial impact of repairs to the A40 remain a major impact should the PSA fail; however, the road is now used by an average of nearly 30,000 vehicles on any given day of the year (2019 value; see Fig. 2). Based on UK average hourly use, this equates to in excess of 2000 vehicles using the A40 at Leys Bend per hour at peak times. Considering historic displacement data alone, the case for direct intervention to remediate the PSA is not strong. However, with the effects of a changing climate and increased road use acting to increase the probability of failure and increase the exposure of elements at risk respectively, the case for
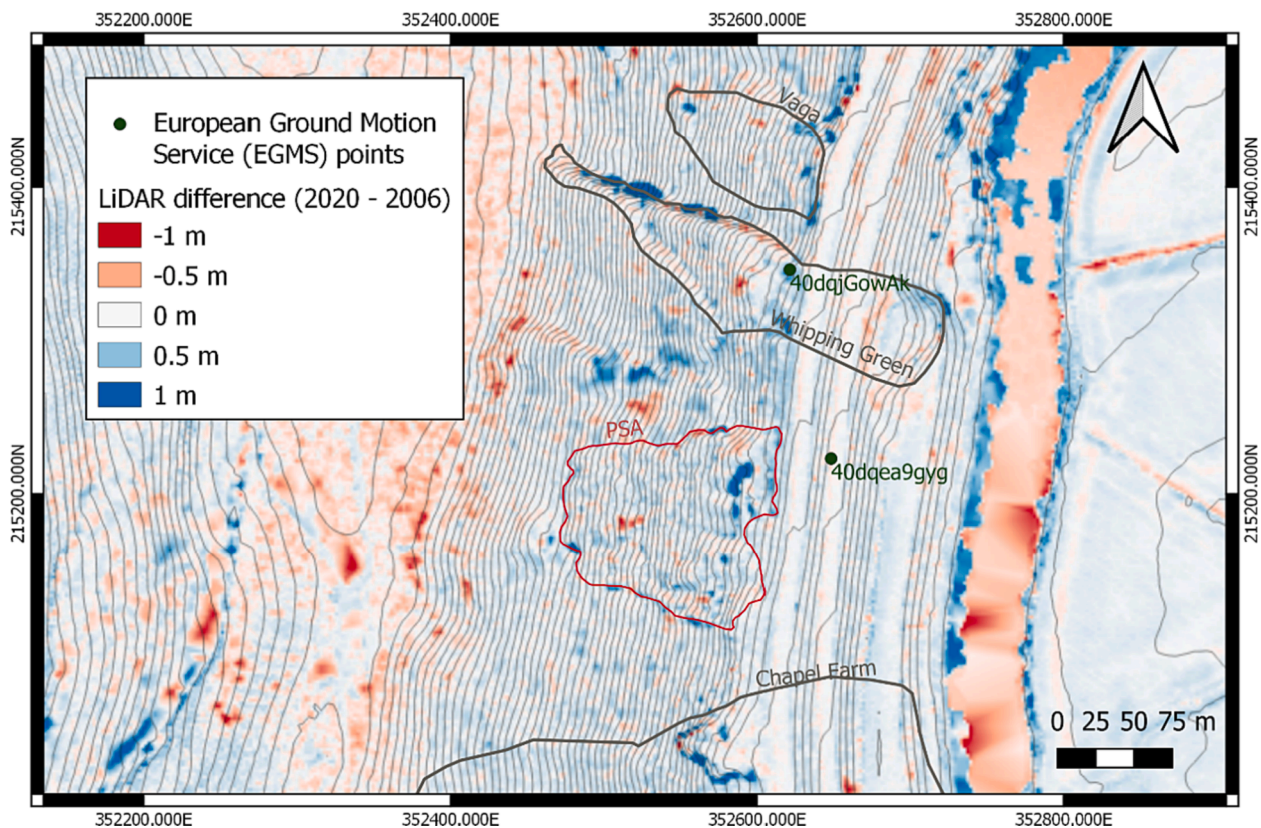
Fig. 9. LiDAR difference plot between 2020 and 2006, showing areas of accumulation (blue) and ablation (red). Contains Department for Environment Food & Rural Affairs material © Crown copyright and database rights [2022]. (For interpretation of the references to colour in this figure legend, the reader is referred to the web version of this article.)
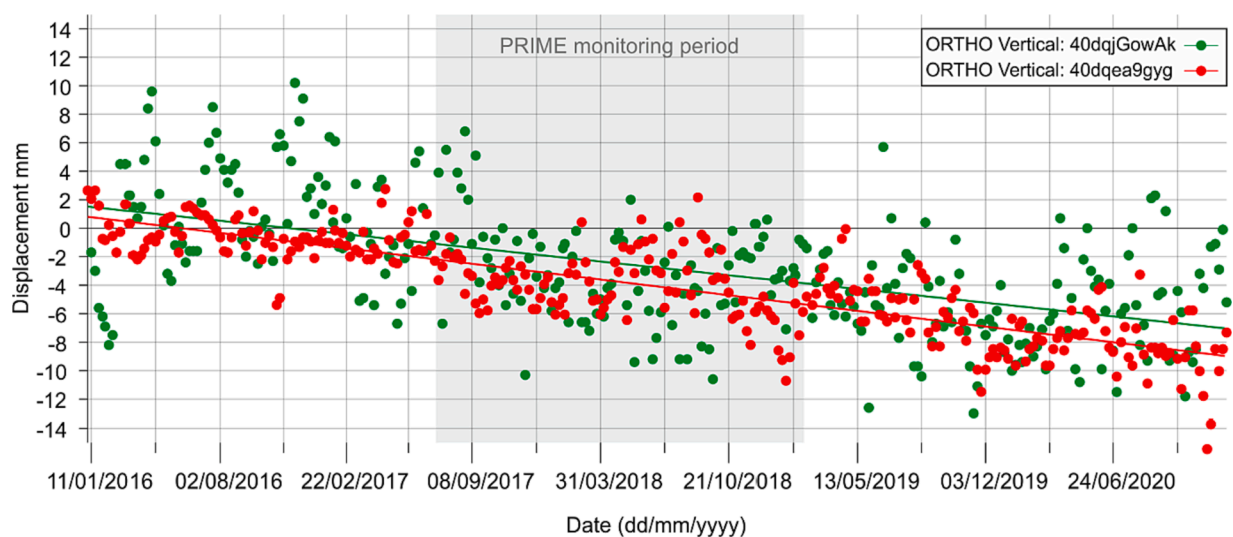

Fig. 10. Vertical deformation measurements from European Ground Motion Service points located near to the PSA at Leys Bend (Fig. 9). © European Union, Copernicus Land Monitoring Service [2022], European Environment Agency (EEA).

continued monitoring of the site is much stronger.

Conclusions

Time-lapse resistivity monitoring of the PSA at Leys Bend has provided information on both the geological character of the slope and behaviour of moisture dynamics that have the potential to cause slope failure. The baseline models from the resistivity monitoring time-series show a highly heterogeneous subsurface within the PSA but also confirm the depth of the unstable mass. These results refine estimates of the volume of the PSA to $2.7–6.75 \times 10^6 \, \text{m}^3$, placing them at the larger end of initial volume calculations (based on depth estimates by [31] of $4.72–6.07 \times 10^6 \, \text{m}^3$. This refined volume could be used to improve modelling of runout length in the event of a slope failure, similar to those observed at Whipping Green and Chapel Farm.

The resistivity time-series highlights the impact that both variable

slope angle and hummocky terrain, combined with a complex subsurface slip mosaic, have on the runoff, infiltration, storage and drainage characteristics of the PSA compared to stable areas of the slopes at Leys Bend. Complementary geophysical techniques, such as seismic surveying, could provide information on the different degrees of fracturing within localised areas of the PSA. Although the resistivity monitoring highlights the variable moisture dynamics of the site, it has also been used to indicate that no movement has occurred in the monitoring period. This is corroborated by both LiDAR change models and ground motion data, both of which were acquired from publicly available sources. Although the PSA at Leys Bend shows no significant signs of surface displacement, time-lapse resistivity models reveal dynamic subsurface moisture-driven processes at the site. Given the relatively short times from significant displacement onset to catastrophic failure at the site in the past (just four days at the Chapel Farm landslide), time-lapse resistivity provides a means of monitoring the precursory moisture conditions that may drive future slope failures at Leys Bend, and underscores the importance of considering slope-scale, subsurface data when executing long-term mitigation strategies at low activity, high risk landslide sites.

CRediT authorship contribution statement

Jim Whiteley: Investigation, Writing – original draft, Writing – review & editing, Visualization. **Cornelia Inauen:** Methodology, Software, Investigation, Writing – review & editing. **Paul Wilkinson:** Conceptualization, Methodology, Software, Investigation, Writing – review & editing. **Philip Meldrum:** Conceptualization, Methodology, Investigation. **Russell Swift:** Methodology, Investigation. **Oliver Kuras:** Conceptualization, Supervision. **Jonathan Chambers:** Conceptualization, Methodology, Investigation, Supervision.

Declaration of Competing Interest

The authors declare that they have no known competing financial interests or personal relationships that could have appeared to influence the work reported in this paper.

Data availability

Data will be made available on request.

Acknowledgements

References

[1] Loke MH, Chambers JE, Rucker DF, Kuras O, Wilkinson PB. Recent developments in the direct-current geoelectrical imaging method. J Appl Geophys 2013;95: 135–56. https://doi.org/10.1016/j.jappgeo.2013.02.017.

[2] Slater L, Binley A. Advancing hydrological process understanding from long-term resistivity monitoring systems. WIREs Water 2021;8. https://doi.org/10.1002/wat2.1513.

[3] Swift RT, Chambers JE, Wilkinson PB, Inauen C, Boyd J, Mtangadura T. et al. Daily monitoring of hydrodynamics under conservation agriculture using electrical resistivity tomography. AGU Fall Meeting 2021, 2021. AGU.

[4] Cimpoiaşu MO, Kuras O, Pridmore T, Mooney SJ. Potential of geoelectrical methods to monitor root zone processes and structure: A review. Geoderma 2020; 365. https://doi.org/10.1016/j.geoderma.2020.114232.

[5] Chambers J, Meldrum P, Wilkinson P, Gunn D, Watlet A, Dashwood B, et al., 2021. Geophysical remote condition monitoring of transportation infrastructure slopes. 2021, 1-5.https://doi.org/10.3997/2214-4609.202120077.

[6] Mclachlan P, Chambers J, Uhlemann S, Sorensen J, Binley A. Electrical resistivity monitoring of river–groundwater interactions in a chalk river and neighbouring riparian zone. Near Surface Geophys 2020;18:385–98. https://doi.org/10.1002/nsg.12114.

[7] Johnson TC, Burghardt J, Strickland C, Knox H, Vermeul V, White M, et al. 4d proxy imaging of fracture dilation and stress shadowing using electrical resistivity tomography during high pressure injections into a dense rock formation. J Geophys Res: Solid Earth 2021;126: e2021JB022298. https://doi.org/10.1029/2021JB022298.

[8] Glaser DR, Henderson RD, Werkema DD, Johnson TJ, Versteeg RJ. Estimating biofuel contaminant concentration from 4d ert with mixing models. J Contam Hydrol 2022;248. https://doi.org/10.1016/j.jconhyd.2022.104027.

[9] Dimech A, Cheng L, Chouteau M, Chambers J, Uhlemann S, Wilkinson P, et al. A review on applications of time-lapse electrical resistivity tomography over the last 30 years : Perspectives for mining waste monitoring. Surv Geophys 2022. https://doi.org/10.1007/s10712-022-09731-2.

[10] Whiteley JS, Chambers JE, Uhlemann S, Wilkinson PB, Kendall JM. Geophysical monitoring of moisture-induced landslides: A review. Rev Geophys 2019;57: 106–45. https://doi.org/10.1029/2018rg000603.

[11] Whiteley JS, Watlet A, Kendall JM, Chambers JE. Brief communication: The role of geophysical imaging in local landslide early warning systems. Nat Hazards Earth Syst Sci 2021;21:3863–71. https://doi.org/10.5194/nhess-21-3863-2021.

[12] Whiteley JS, Chambers JE, Uhlemann S, Boyd J, Cimpoiasu MO, Holmes JL, et al. Landslide monitoring using seismic refraction tomography – the importance of incorporating topographic variations. Eng Geol 2020;268. https://doi.org/10.1016/j.enggeo.2020.105525.

[13] Bainbridge R, Lim M, Dunning S, Winter MG, Diaz-Moreno A, Martin J, et al., 2022. Detection and forecasting of shallow landslides: Lessons from a natural laboratory. *Geomatics, Natural Hazards and Risk,* 13, 686-704.10.1080/19475705.2022.2041108.

[14] Whiteley JS, Watlet A, Uhlemann S, Wilkinson P, Boyd JP, Jordan C, et al. Rapid characterisation of landslide heterogeneity using unsupervised classification of electrical resistivity and seismic refraction surveys. Eng Geol 2021. https://doi.org/10.1016/j.enggeo.2021.106189.

[15] Holmes J, Chambers J, Meldrum P, Wilkinson P, Boyd J, Williamson P, et al. Four-dimensional electrical resistivity tomography for continuous, near-real-time monitoring of a landslide affecting transport infrastructure in british columbia, canada. Near Surface. Geophysics 2020;18:337–51. https://doi.org/10.1002/nsg.12102.

[16] Kuras O, Pritchard JD, Meldrum PI, Chambers JE, Wilkinson PB, Ogilvy RD, et al. Monitoring hydraulic processes with automated time-lapse electrical resistivity tomography (alert). C R Geosci 2009;341:868–85. https://doi.org/10.1016/j.crte.2009.07.010.

[17] Supper R, Romer A, Kreuzer G, Jochum B, Ottowitz D, Ita Aet al. *The geomon 4d electrical monitoring system: Current state and future developments;* 2012.

[18] Tresoldi G, Arosio D, Hojat A, Longoni L, Papini M, Zanzi L. Long-term hydrogeophysical monitoring of the internal conditions of river levees. Eng Geol 2019;259. https://doi.org/10.1016/j.enggeo.2019.05.016.

[19] Watlet A, Thirugnanam H, Singh B, Kumar MN, Brahmanandan D, Inauen C, et al. 4d electrical resistivity to monitor unstable slopes in mountainous tropical regions: An example from munnar, india. *Landslides,* 2023;20:1031–1044. 10.1007/s10346-023-02029-3.

[20] Chambers J, Holmes J, Whiteley J, Boyd J, Meldrum P, Wilkinson P, et al. Long-term geoelectrical monitoring of landslides in natural and engineered slopes. Lead Edge 2022;41:768–76. https://doi.org/10.1190/tle41110768.1.

[21] Holmes J, Chambers J, Wilkinson P, Meldrum P, Cimpoiaşu M, Boyd J, et al. Application of petrophysical relationships to electrical resistivity models for assessing the stability of a landslide in british columbia, canada. Eng Geol 2022. https://doi.org/10.1016/j.enggeo.2022.106613.

[22] Wilkinson PB, Uhlemann S, Chambers JE, Meldrum PI, Loke MH. Development and testing of displacement inversion to track electrode movements on 3-d electrical resistivity tomography monitoring grids. Geophys J Int 2015;200:1566–81. https://doi.org/10.1093/gji/ggu483.

[23] Wilkinson P, Chambers J, Uhlemann S, Meldrum P, Smith A, Dixon N, et al. Reconstruction of landslide movements by inversion of 4-d electrical resistivity tomography monitoring data. Geophys Res Lett 2016;43:1166–74. https://doi.org/10.1002/2015gl067494.

[24] Froude MJ, Petley DN. Global fatal landslide occurrence from 2004 to 2016. Nat Hazards Earth Syst Sci 2018;18:2161–81. https://doi.org/10.5194/nhess-18-2161-2018.

[25] Terzaghi K. *Theoretical soil mechanics*, J. Wiley and Sons inc.; 1943.

[26] Marino P, Peres DJ, Cancelliere A, Greco R, Bogaard TA. Soil moisture information can improve shallow landslide forecasting using the hydrometeorological threshold approach. Landslides 2020;17:2041–54. https://doi.org/10.1007/s10346-020-01420-8.

[27] Wicki A, Jansson PE, Lehmann P, Hauck C, Stähli M. Simulated or measured soil moisture: Which one is adding more value to regional landslide early warning? Hydrol Earth Syst Sci 2021;25:4585–610. https://doi.org/10.5194/hess-25-4585-2021.

[28] Felsberg A, De Lannoy GJM, Girotto M, Poesen J, Reichle RH, Stanley T. Global soil water estimates as landslide predictor: The effectiveness of smos, smap, and grace observations, land surface simulations, and data assimilation. J Hydrometeorol 2021;22:1065–84. https://doi.org/10.1175/jhm-d-20-0228.1.

[29] Koyama CN, Liu H, Takahashi K, Shimada M, Watanabe M, Khuut T, et al. In-situ measurement of soil permittivity at various depths for the calibration and validation of low-frequency sar soil moisture models by using gpr. Remote Sens (Basel) 2017;9:580.

[30] Ramesh MV. Design, development, and deployment of a wireless sensor network for detection of landslides. *Ad Hoc Networks,* 2014;13, Part A**,** 2-18. https://doi.org/10.1016/j.adhoc.2012.09.002.

[31] Early KR, Jordan PG. Some landslipping encountered during construction of the a40 near monmouth. Q J Eng Geol Hydrogeol 1985;18:207–24. https://doi.org/10.1144/gsl.qjeg.1985.018.03.03.

[32] Smedley MI, Paulson R, Tucker A. Remote sensing for highway management of landslides. Proc Inst Civil Eng - Geotech Eng, 2009;162:141-150. 10.1680/geng.2009.162.3.141.

[33] Hansard. HC Deb. vol. 761, 27 March 1968. [Online]. Available: https://hansard.parliament.uk/Commons/1968-03-27 [Accessed 23/06/2022].

[34] Weatherunderground. 2023. *The hendre - 5km w of monmouth - igwentmo3* [Online]. Available: https://www.wunderground.com/dashboard/pws/IGWENTMO3 [Accessed 2017].

[35] Hargreaves GH, Samani ZA. Estimating potential evapotranspiration. J Irrig Drain Div 1982;108:225–30. https://doi.org/10.1061/JRCEA4.0001390.

[36] Samani Z. Estimating solar radiation and evapotranspiration using minimum climatological data. J Irrig Drain Eng 2000;126:265–7. https://doi.org/10.1061/(ASCE)0733-9437(2000)126:4(265).

[37] Uhlemann S, Chambers J, Wilkinson P, Maurer H, Merritt A, Meldrum P, et al. Four-dimensional imaging of moisture dynamics during landslide reactivation. J Geophys Res Earth 2017;122:398–418. https://doi.org/10.1002/2016JF003983.

[38] Labrecque D, Miletto M, Daily W, Ramirez A, Owen E. The effects of noise on occam's inversion of resistivity tomography data. Geophysics 1996;61:538–48. https://doi.org/10.1190/1.1443980.

[39] Tso C-H-M, Kuras O, Wilkinson PB, Uhlemann S, Chambers JE, Meldrum PI, et al. Improved characterisation and modelling of measurement errors in electrical resistivity tomography (ert) surveys. J Appl Geophys 2017;146:103–19. https://doi.org/10.1016/j.jappgeo.2017.09.009.

[40] Wilkinson PB, Chambers JE, Meldrum PI, Kuras O, Inauen CM, Swift RT, et al. Windowed 4d inversion for near real-time geoelectrical monitoring applications. Front Earth Sci 2022;10. https://doi.org/10.3389/feart.2022.983603.

[41] Loke M, Dahlin T, Rucker D. Smoothness-constrained time-lapse inversion of data from 3d resistivity surveys. Near Surf Geophys 2014;12:5–24. https://doi.org/10.3997/1873-0604.2013025.

[42] Lesparre N, Nguyen F, Kemna A, Robert T, Hermans T, Daoudi M, et al. A new approach for time-lapse data weighting in electrical resistivity tomography. Geophysics 2017;82:E325–33. https://doi.org/10.1190/GEO2017-0024.1.

[43] Singha K, Day-Lewis F, Johnson T, Slater L. Advances in interpretation of subsurface processes with time-lapse electrical imaging. Hydrol Process 2015;29:1549–76. https://doi.org/10.1002/hyp.10280.

[44] Chambers J, Gunn D, Wilkinson P, Meldrum P, Haslam E, Holyoake S, et al. 4d electrical resistivity tomography monitoring of soil moisture dynamics in an operational railway embankment. Near Surf Geophys 2014;12:61–72. https://doi.org/10.3997/1873-0604.2013002.

[45] Chretien M, Lataste J, Fabre R, Denis A. Electrical resistivity tomography to understand clay behavior during seasonal water content variations. Eng Geol 2014;169:112–23. https://doi.org/10.1016/j.enggeo.2013.11.019.

[46] Brunet P, Clement R, Bouvier C. Monitoring soil water content and deficit using electrical resistivity tomography (ert) - a case study in the cevennes area, france. J Hydrol 2010;380:146–53. https://doi.org/10.1016/j.jhydrol.2009.10.032.

[47] Hayashi M. Temperature-electrical conductivity relation of water for environmental monitoring and geophysical data inversion. Environ Monit Assess 2004;96:119–28. https://doi.org/10.1023/B:EMAS.0000031719.83065.68.

[48] Hayley K, Bentley LR, Gharibi M, Nightingale M. Low temperature dependence of electrical resistivity: Implications for near surface geophysical monitoring. Geophys Res Lett 2007;34, -.Artn L18402 Doi 10.1029/2007gl031124.

[49] Wilkinson PB, Chambers JE, Meldrum PI, Gunn DA, Ogilvy RD, Kuras O. Predicting the movements of permanently installed electrodes on an active landslide using time-lapse geoelectrical resistivity data only. Geophys J Int 2010;183:543–56. https://doi.org/10.1111/j.1365-246X.2010.04760.x.

[50] Colesanti C, Wasowski J. Investigating landslides with space-borne synthetic aperture radar (sar) interferometry. Eng Geol 2006;88:173–99. https://doi.org/10.1016/j.enggeo.2006.09.013.

[51] Kelevitz K, Novellino A, Watlet A, Boyd J, Whiteley J, Chambers J, et al. Ground and satellite-based methods of measuring deformation at a uk landslide observatory: Comparison and integration. Remote Sens (Basel) 2022;14:2836.

[52] Gibson AD, Culshaw MG, Dashwood C, Pennington CVL. Landslide management in the uk—the problem of managing hazards in a 'low-risk' environment. Landslides 2013;10:599–610. https://doi.org/10.1007/s10346-012-0346-4.

[53] Ahrens J, Geveci B, Law C. Paraview: An end-user tool for large data visualization. Visualization Handbook; 2005.